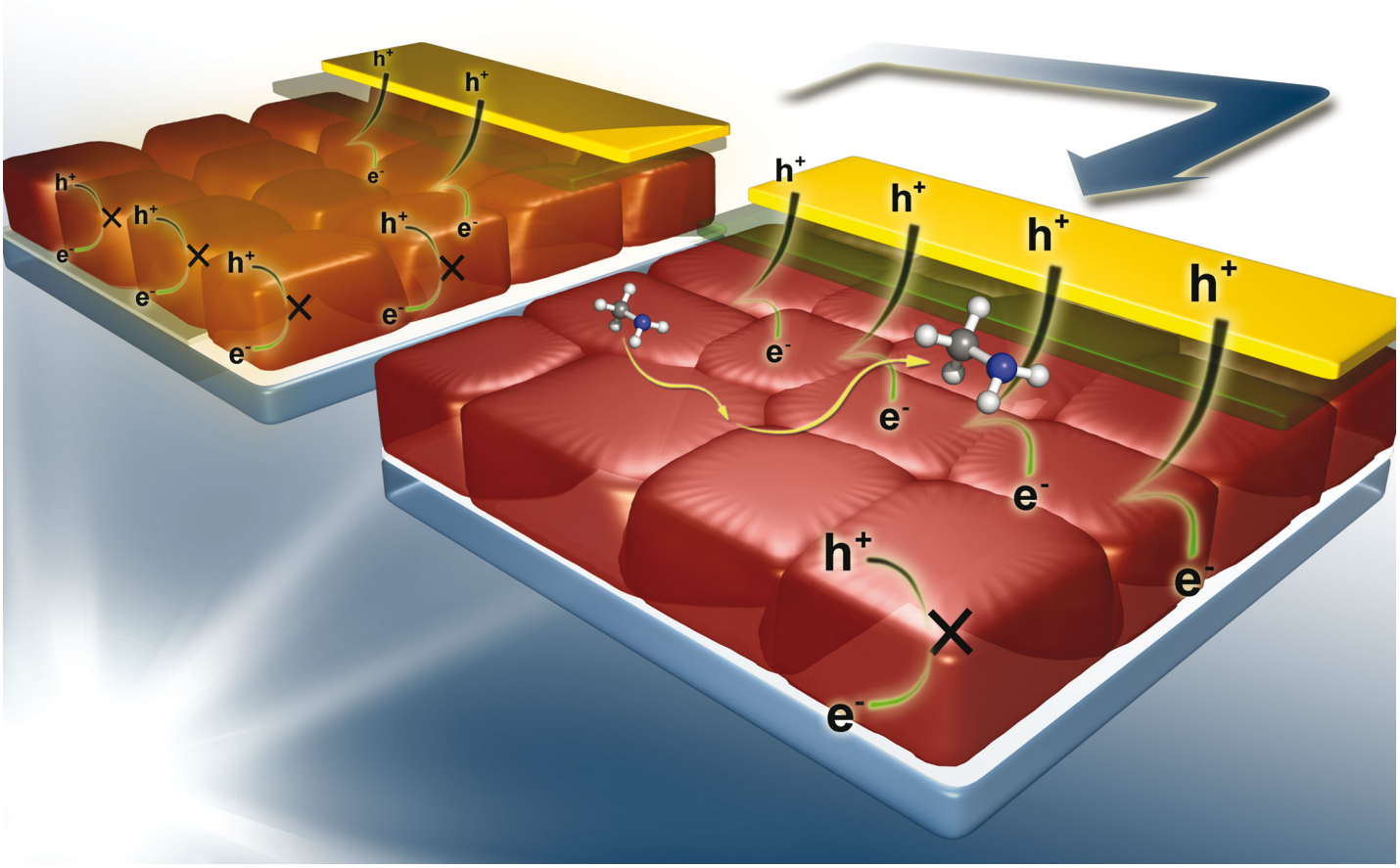

Showcasing the enhanced performance and stability of perovskite solar cells by methylamine post-annealing by Prof. Yabing Qi at the Energy Materials and Surface Sciences Unit (EMSS) in the Okinawa Institute of Science and Technology Graduate University (OIST).

Post-annealing of $MAPbI_3$ perovskite films with methylamine for efficient perovskite solar cells

Methylamine post-annealing solves the grain boundary-related issues and suppresses both inter- and intra-layer carrier recombination in $MAPbI_3$ perovskite films. Both planar and meso-structured perovskite solar cells with methylamine post-annealing show better performance and stability compared to other post-annealing treatments.

As featured in:

See Yabing Qi *et al.*, *Mater. Horiz.*, 2016, **3**, 548.

ROYAL SOCIETY OF CHEMISTRY

rsc.li/materials-horizons

Registered charity number: 207890

Materials Horizons

COMMUNICATION

View Article Online
View Journal | View Issue

Cite this: *Mater. Horiz.*, 2016, 3, 548

Received 24th May 2016,
Accepted 5th August 2016

DOI: 10.1039/c6mh00160b

www.rsc.li/materials-horizons

Post-annealing of $MAPbI_3$ perovskite films with methylamine for efficient perovskite solar cells†

Yan Jiang,[a] Emilio J. Juarez-Perez,[a] Qianqing Ge,[b] Shenghao Wang,[a] Matthew R. Leyden,[a] Luis K. Ono,[a] Sonia R. Raga,[a] Jinsong Hu[b] and Yabing Qi*[a]

An organo-metal halide perovskite is a promising material for solar cell applications, but the polycrystalline nature of perovskites can cause thin films to be non-uniform with disconnected grains. These grain boundaries make the perovskite film vulnerable to the local chemical environment, or allow unwanted direct contact of the electron transporting layer and the hole transporting layer, increasing carrier recombination. We show that post-annealing with methylamine greatly reduces impurities at perovskite grain boundaries and promotes continuity between adjacent grains. When methylamine post-annealed perovskite films are compared to thermally or solvent-annealed films, the carrier lifetime is increased by 3 times. The recombination resistance for the planar perovskite solar cells with the methylamine post-annealing treatment is increased more than 10 times, and the efficiency is increased by 43.1% and 20.0% with respect to the thermally annealed and solvent-annealed perovskite solar cells, respectively. In addition, we show that methylamine post-annealed, meso-structured perovskite solar cells exhibited a power conversion efficiency of up to 18.4%, with significantly improved stability.

Conceptual insights

The quality of perovskite films is one of the most important influencing factors for perovskite solar cells. We develop a methylamine post-annealing treatment to improve the performance of a $MAPbI_3$ perovskite solar cell. This method is shown to significantly improve grain boundary (GB)-related issues as compared to thermal annealing and solvent annealing. The control experiments of pure ethanol post-annealing on $MAPbI_3$ confirm that the major improvement is indeed a result of the methylamine post-annealing, but not an effect of ethanol solvent annealing alone. Our results show that (I) surface impurities at GBs are significantly reduced and carrier recombination within the perovskite layer is suppressed; (II) disconnected grains are avoided and the direct contact between the electron transporting layer and the hole transporting layer is nearly eliminated, thus carrier recombination between separate layers is suppressed. The detailed study on these two separated carrier recombination processes provides valuable guidelines for recombination kinetics analyses. Perovskite solar cell device results show that methylamine post-annealing significantly improves not only device efficiency but also stability, independent of device architecture. Furthermore, methylamine post-annealing is easy to process and highly reproducible, which is expected to be applicable for perovskite films prepared by different fabrication methods.

Introduction

Organo-lead-halide perovskite (OHP)-based materials have achieved great success in photovoltaic applications because of their excellent optoelectronic properties and easy processability.[1–9] Significant breakthroughs have been achieved in the past few years with the latest certified power conversion efficiency (PCE) of 22.1%,[10] which is comparable to that of crystalline silicon solar cells. The quality of perovskite films is one of the most important factors influencing the performance of perovskite solar cells.[11–13] Thus, much work has been devoted to controlling perovskite formation kinetics, *e.g.* adjusting solvent composition[14–17] and the precursor ratio,[18] using additives[19–22] and anti-solvent[23,24] to form pinhole free perovskite layers, and regulating perovskite crystallinity by partially dissolving and recrystallizing perovskites to form large crystal domains to enhance charge extraction.[25–27]

However, because of the polycrystalline nature of perovskite layers, cracks in the periodic crystal structure lead to the formation of a large number of grain boundaries (GBs). These grain boundaries are generally thought to have a negative impact on device performance, despite reports in which GBs showed higher photocurrent based upon c-AFM measurements.[28,29] This higher current at GBs may be related to ion migration-induced doping.[30] However, to date, no studies have shown that more grain boundaries result in better device performance. On the other hand, the many trap states existing at GBs are likely to act

[a] *Energy Materials and Surface Sciences Unit (EMSS), Okinawa Institute of Science and Technology Graduate University (OIST), 1919-1 Tancha Onna-son, Okinawa 904-0495, Japan. E-mail: Yabing.Qi@OIST.jp*

[b] *CAS Key Laboratory of Molecular Nanostructure and Nanotechnology, Institute of Chemistry, Chinese Academy of Sciences (CAS), Beijing 100190, P. R. China*

† Electronic supplementary information (ESI) available: Experimental details (solar cell fabrication, perovskite film characterization, and solar cell device characterization), Fig. S1–S15 and Tables S1–S3. See DOI: 10.1039/c6mh00160b

as non-radiative recombination centers, reducing the carrier separation efficiency.[31,32] These areas are also more vulnerable to the local chemical environment.[33] Therefore, further treatment for defect passivation or surface impurity elimination at GBs is critically important.[34] However, the most widely used post-annealing treatments for solution-processed perovskite solar cells are likely to create disconnected grains during the evaporation of residual solvent, leading to the potential risk of carrier recombination by direct contact between the electron-transporting layer (ETL) and the hole-transporting layer (HTL).[35] Even though the foregoing issues are critical for the device PCE, they have yet to be solved. In the most promising work to date, Cui *et al.* and Zhao *et al.* exposed $MAPbI_3$ perovskite to methylamine gas.[36–39] Disconnected grains were significantly fused by the fast, reversible reaction between $MAPbI_3$ and CH_3NH_2. Nevertheless, use of a gas phase of methylamine makes it difficult to control the amount of reactants, so scale-up could be challenging.

Unlike methylamine gas exposure, here we use a methylamine post-annealing (MPA) treatment for $MAPbI_3$ perovskite. The MPA process is different for three important reasons. (I) In the methylamine gas exposure process, the film is pre-annealed, but in our process treatment occurs during annealing. This means that the residual solvent (*e.g.* DMF and DMSO) evaporates from the perovskite film in a methylamine gas atmosphere during annealing. This greatly improves both inward and outward diffusion of methylamine during perovskite formation, leading to large area uniformity. (II) The reaction kinetic rate constant increases by orders of magnitude because of an increase in reaction temperature, according to the Arrhenius equation; thus, the fusing effect of methylamine is significantly increased. (III) A solution-based precursor where methylamine is dissolved in ethanol is simpler to control than the methylamine gas-based process, which facilitates scale-up. Further comparisons are made with the MPA process and other annealing processes that are widely used for perovskite fabrication, specifically thermal annealing (TA) and DMF solvent annealing (SA).[25,40] We find that many GB-related issues are solved with methylamine post-annealing treatment, compared to other annealing methods. (I) Surface impurities at GBs are greatly reduced; thus, the carrier recombination within perovskite layers (defined as intra-layer carrier recombination) is suppressed. (II) Disconnected grains that would otherwise be formed during residual solvent evaporation are avoided and the chance of direct contact between the ETL and HTL is nearly eliminated, therefore the carrier recombination between separate layers (defined as inter-layer carrier recombination) is restrained. With these advantages, the mean device performance of planar perovskite solar cells (PSC) with MPA treatment improved 43.1% over TA-treated and 20.0% over SA-treated perovskite solar cells. We also show that the MPA treatment is not only suitable for planar PSCs, but is also applicable for meso-structured PSCs, which reach a power conversion efficiency as high as 18.4%.

Result and discussion

Five different procedures for perovskite layer formation are used in this study and details are presented in the Experimental section (ESI†). The first method attempted is methylamine solution exposure (MSE), where an ethanolic methylamine solution is used as a precursor, and methylamine solution concentration is varied to control the reaction rate.[41] The intensity of the X-ray diffraction (XRD) peak at 14.1°, corresponding to the (110) perovskite crystal plane, consistently increases with the amount of methylamine solution exposure (Fig. S1, ESI†), suggesting that better perovskite crystallinity can be achieved with higher methylamine partial pressure during exposure. However, the absorbance of perovskite films (Fig. S2, ESI†) decreases with increasing amount of MSE, especially for photon wavelengths less than 500 nm. Uniformity of the films also deteriorates by increasing the amount of MSE, as seen in pictures of samples (inset, Fig. S2, ESI†). The optimized MSE amount is 0.5 mL. However, uniformity remains a problem even with the optimal amount of methylamine solution, and the resulting average PCE of planar PSCs showed large variation with little improvement (Fig. S3, ESI†). To overcome these difficulties, a new methodology of methylamine post-annealing treatment for $MAPbI_3$ perovskite was developed and is compared herein to previously reported TA and SA treatments.[25,40] Because an ethanolic methylamine solution is used for the post-annealing, additional control experiments based on pure ethanol post-annealing on perovskite is conducted to clarify the role of methylamine and ethanol.

Different procedures for perovskite layer preparation were employed, details of which are described in the Experimental section (Fig. 1). In brief, $MAPbI_3$ perovskite layers were spin-coated on FTO/compact TiO_2 layers using the anti-solvent method[23] with different post-annealing procedures, *i.e.* thermal annealing, DMF solvent annealing and methylamine post-annealing, which are designated as TA, SA and MPA, respectively. The same procedure was also conducted for the preparation of ethanol post-annealed perovskite films. Morphologies of perovskite films before and after various post-annealing treatments were first investigated using scanning electron microscopy (SEM). The unannealed film shows nanobranch structures with a branch width of ~150 nm (Fig. S4, ESI†). After various post-annealing, all four perovskite films show good coverage without any pinholes, in good agreement with previous work using the anti-solvent method[23] (Fig. 2a–c and Fig. S5, ESI†). The grain size of SA treated films is substantially larger than those of TA or MPA, which are similar. From high magnification SEM images,

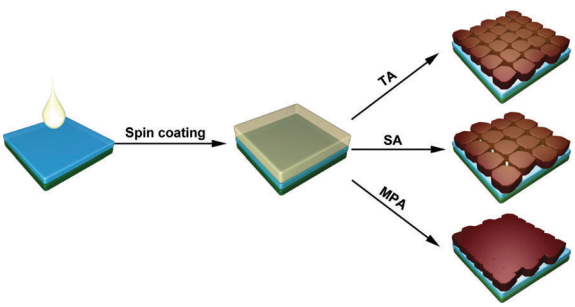

Fig. 1 Schematics of perovskite film preparation with thermal annealing (TA), DMF solvent annealing (SA), and methylamine post-annealing treatment (MPA).

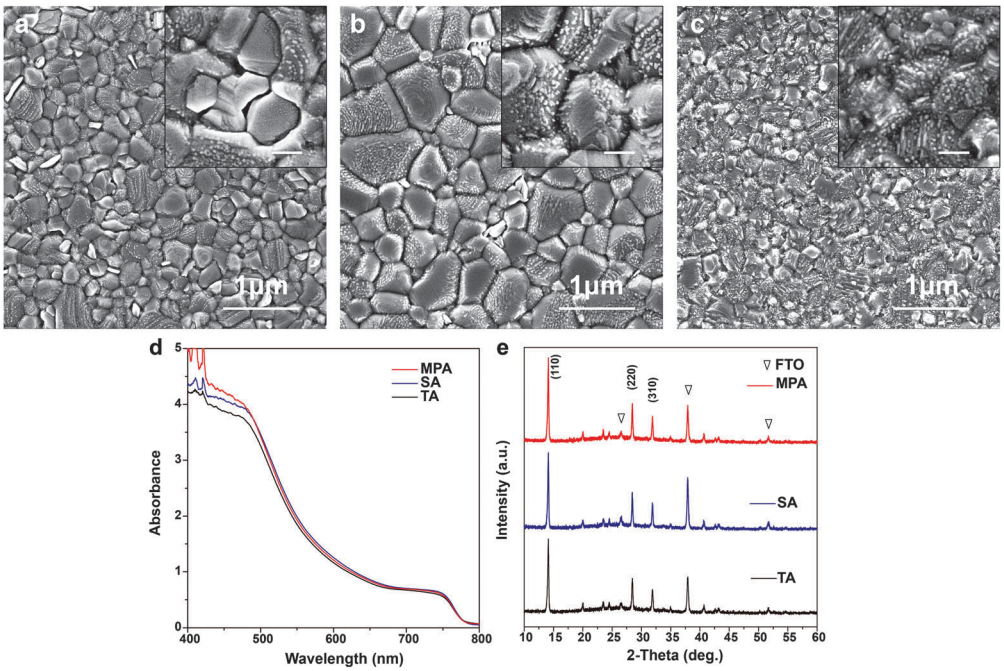

Fig. 2 SEM images of the $MAPbI_3$ perovskite films with thermal annealing (a), DMF solvent annealing (b) and methylamine post-annealing (c) treatments. High-magnification SEM images are shown in the insets, with scale bars representing 200 nm. UV-vis spectra (d) and XRD patterns (e) of $MAPbI_3$ films with various post-annealing treatments. Methylamine post-annealing promotes greater continuity between adjacent grains, compared to solvent and thermal annealing.

it is clear that perovskite films prepared using the TA and SA treatments show deep gaps between adjacent grains. However, for the MPA-treated perovskite film, grains are merged to form a continuous surface. No obvious morphology differences can be found between thermally- and ethanol post-annealed samples (Fig. S5, ESI†). Root mean square (RMS) surface roughness is also measured using atomic-force microscopy (AFM) and is determined to be 11.3 nm, 21.7 nm, and 10.3 nm, respectively, for TA-, SA- and MPA-treated films for an area of 5 × 5 μm.[42] Although a perovskite layer with a large grain size can be obtained using SA treatment, gaps between grains are also more likely to occur, increasing the likelihood of direct contact between the ETL and HTL. In addition, because in the case of MPA treatment the gaps are fused, inter-layer carrier recombination is expected to be significantly reduced. The absorbance spectra of the perovskite films with various post-annealing processes exhibit similar absorbance edges and intensities, except for a slight increase at wavelengths less than 500 nm for the MAP-treated perovskite (Fig. 2d and Fig. S6, ESI†). The composition and structure of the perovskite are characterized using XRD (Fig. 2e and Fig. S7, ESI†). Diffraction peaks at 14.1°, 28.5°, and 31.9° are indexed to be (110), (220), and (310) $CH_3NH_3PbI_3$ crystal planes, and other peaks at 26.6°, 37.9°, 51.7° are assigned to the FTO substrate. All four samples show similar peak positions and intensities. Because grain sizes are larger with the SA-treated film, we expected that the diffraction peaks of the SA-treated perovskite would be slightly narrower than the others.[43] However, after normalizing the perovskite (110) peak intensities, the peak widths at half-maxima are about the same for all samples, meaning that on average, the differences in crystallinity are not significant (Fig. S8, ESI†). This result differs from that in the case of exposure to methylamine solution, which shows a significant improvement in crystallinity (see the XRD data in Fig. S1, ESI†). This crystallinity difference between MSE- and MPA-treated samples shows that the resulting film undergoes significantly different processes.[36]

Because the surface morphology of perovskite films differs with various post-annealing treatments, chemical states of the surface elements are expected to differ compared to bulk perovskites. Different levels of surface impurities could greatly influence the device performance.[41] Thus, high resolution X-ray photoemission spectroscopy (HRXPS) was performed to analyze surface chemical states of perovskite films with TA, SA and MPA regimes. All perovskite films with different post-annealing treatments show two symmetric peaks at 143.4 and 138.6 eV, which are assigned to the Pb $4f_{5/2}$ and Pb $4f_{7/2}$ peaks, respectively (Fig. 3a). These peaks are associated with Pb^{2+} in the perovskite. However, for the TA-treated film, another pair of peaks with low binding energies (141.6 and 136.8 eV) was also detected by surface-sensitive XPS measurements. These are associated with Pb^0 and cannot be detected using XRD.[44,45] The results suggest that metallic lead (Pb^0) impurities do not exist on SA- and MPA-treated perovskite film surfaces. For all the post-annealed perovskite films, two peaks at 286.4 and 285.1 eV are assigned to C 1s peaks (Fig. 3b). The higher energy peak at 286.4 eV comes from $CH_3NH_3^+$ in the perovskite and the lower energy peak at 285.1 eV is associated with some non-perovskite species formed at perovskite GBs.[46,47] The intensity ratio between the

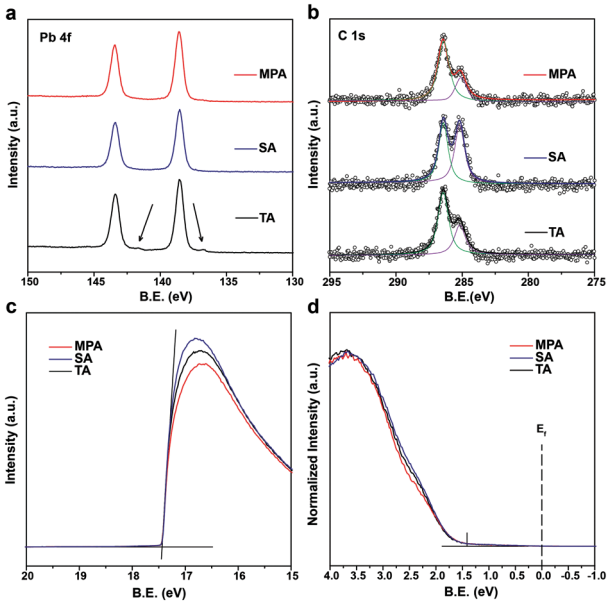

Fig. 3 (a) Pb 4f, (b) C 1s HRXPS spectra and (c) cut-off energy region, (d) valence band region of UPS spectra of $MAPbI_3$ perovskite films with various post-annealing treatments. MPA-treated films show fewer surface impurities than TA- and SA-treated films.

two peaks (α = area of low energy peak/area of high energy peak) indicates the amount of carbon-related impurities at perovskite GBs. α increases from 0.567 for the TA-treated perovskite to 1.102 for the SA-treated perovskite, but is greatly reduced (0.350) in the MPA-treated perovskite, demonstrating that carbon related impurities have been significantly removed during the MPA treatment. In addition, the intensity of the O 1s peak is reduced for the MPA-treated perovskite compared to the TA- and SA-treated samples (Fig. S9, ESI†). Little difference is seen in the I 3d and N 1s spectra (Fig. S9, ESI†). Because oxygen is not an intrinsic element in perovskite, the probing of oxygen in HRXPS may be due to the surface oxidation of perovskite. MPA-treated perovskite films show lower levels of oxygen-related surface impurities.[40,48] The significantly reduced amount of lead-, carbon- and oxygen-related impurities in the MPA-treated samples is consistent with the minimized deep gaps in such samples. It is well known that surface impurities are likely to act as non-radiative recombination centers. Therefore, it is expected that intra-layer charge recombination will be suppressed by the MPA treatment, which will lead to improved PCEs of perovskite solar cells. Ultraviolet photoemission spectroscopy (UPS) is also performed to measure the work function and the valence band edge of perovskite films with TA, SA and MPA treatments. The secondary electron cut-off energy and the valence band edge are similar for the three samples, suggesting that the various post-annealing treatments do not affect surface energy levels of the different perovskites at the macroscopic scale (Fig. 3c and d). Therefore, similar energy level alignments are matched between the perovskite and the HTL for all devices. This result is further proven by the valence band spectra from the XPS measurements (Fig. S10, ESI†). The valence band edge is located at 1.4 eV below the Fermi level as shown in the logarithmic scale representation of the UPS valence region (Fig. S11, ESI†), which is in good agreement with the literature.[49]

Photovoltaic devices were fabricated with perovskite films prepared using TA, SA, MPA and ethanol post-annealing treatments to evaluate the influence of disconnected grains and surface impurities on device performance. Planar devices with FTO/c-TiO_2/$MAPbI_3$/spiro-MeOTAD/Au are fabricated and labeled with the superscript a (Fig. S12, ESI†). Photocurrent–voltage (J–V) characteristics of the champion cells with TA, SA and MPA treatments show that the device PCEs are improved by SA treatment compared to TA treatment, but the best performance comes from MPA treatment (Fig. 4a). All data were collected using forward to reverse scans. A large mismatch in J–V curves exists between the two scan directions (Fig. S13 and Table S1, ESI†). Generally, hysteresis in J–V curves can be reduced either by adding a mesoporous TiO_2 layer on top of the compact TiO_2 layer or by using other electron transporting materials, *e.g.* PCBM, C_{60} and Li-treated mesoscopic TiO_2 *etc.*[50–52] Statistical analysis shows that the PSCs with the MPA treatment exhibited the highest averaged PCE of 15.00%, resulting in a 43.1% and 20.0% improvement compared with the devices employing the TA and SA treatments, respectively (Fig. 4c and Table 1). On the other hand, mean PCEs only slightly increased from 10.5% for thermal annealing to 10.6% for ethanol post-annealing (Fig. S14 and Table S2, ESI†). In contrast to the significant improvement in mean PCEs obtained by MPA (4.5% increase in PCE from 10.5% to 15.0%), the mean PCEs by ethanol post-annealing only marginally increased by 0.1%, indicating that the device

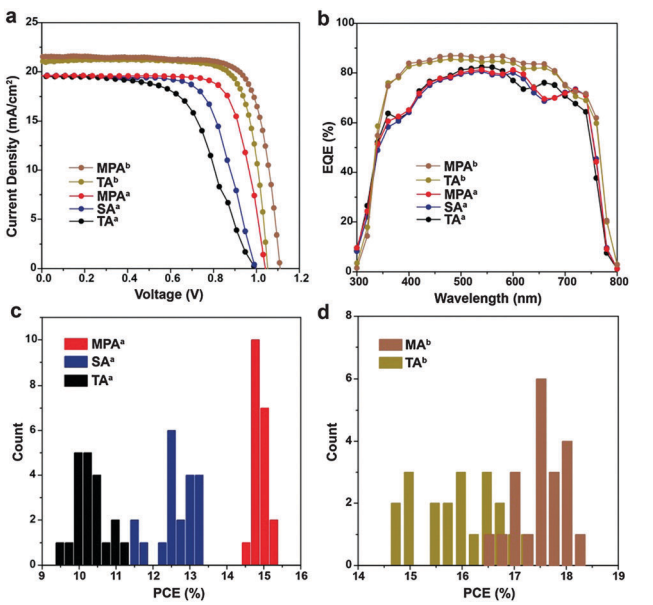

Fig. 4 (a) Photocurrent–voltage (J–V) characteristics, (b) EQE spectra and (c and d) statistical performance of the perovskite solar cells of different structures with various post-annealing treatments. [a] Represents the planar device and [b] represents the meso-structured device. A total of 100 cells (20 cells for each of post-annealing treatments) were considered for the statistical analysis. MPA-treated perovskite solar cells show improved efficiency compared to TA- and SA-treated PSCs.

performance improvement is mainly due to the methylamine post-annealing treatment, but not ethanol post-annealing. The narrower PCE distribution in the case of the MPA treatment also suggests the better reproducibility of this method. Note that the improvement in PCE is thus due to a slightly higher open circuit voltage (V_{oc}) and a significantly higher fill factor (FF), while the short circuit current (J_{sc}) is about the same. This improvement in FF agrees well with the lower charge recombination of the photovoltaic devices.[53,54] To confirm the applicability of the MPA treatment to other solar cell architectures, meso-structured PSCs with TA and MPA treatments are also fabricated by adding a mesoporous TiO_2 layer onto the compact TiO_2 layer and labeled with the superscript b. The device fabrication procedures were slightly changed (see the Experimental section for detail). The champion cells show PCEs of 17.4% for thermally annealed, and 18.4% for methylamine post-annealed PSC (Fig. 4a). Mean PCEs are 16.1% and 17.7% respectively (Fig. 4d and Table 1) suggesting the wide applicability of this method. The degree of hysteresis (DOH) is significantly reduced from 25.0% for the MPA-treated planar PSC to 6.7% for the MPA-treated meso-structured PSC, where DOH is defined as

$$\mathrm{DOH} = \frac{\mathrm{PCE}_{\text{forward to reverse scan}} - \mathrm{PCE}_{\text{reverse to forward scan}}}{\mathrm{PCE}_{\text{forward to reverse scan}}}$$

(Fig. S15 and Table S3, ESI†). The external quantum efficiency (EQE) of the PSCs shows a higher photon-to-current conversion efficiency for the meso-structured PSCs than the planar PSCs. A slightly higher EQE is obtained for the MPA-treated meso-structured PSC compared with the TA-treated meso-structured one (Fig. 4b). Little difference can be seen for the TA-, SA- and MPA-treated PSCs. The integrated current density matched well with the J_{sc} with variations less than 6%.

To experimentally elucidate the relationship between device performance and carrier recombination, time-resolved photoluminescence (TRPL) spectroscopy is performed on the perovskite films with various post-annealing treatments. Perovskite films are prepared on glass substrates. Light pulses of 450 nm are used for excitation and PL decays are recorded at 780 nm. Because no ETL or HTL is used, carrier recombination is considered to represent intra-layer carrier recombination, which is expected to be strongly dependent on the level of impurities at GBs. Instead of using a sum of two or more arbitrary number of exponential functions, here we adopt a more generalized relaxation function to fit TRPL spectra.[55] The time constants τ obtained are 1.74 ± 0.03, 1.86 ± 0.03 and 6.21 ± 0.06 ns for the perovskite films with TA, SA and MPA treatments, respectively (Fig. 5a). This observation means

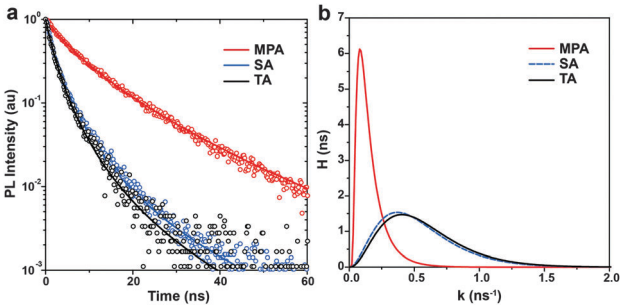

Fig. 5 (a) Time-resolved photoluminescence decay curves and (b) distributions of recombination rate constants of perovskite films with various post-annealing treatments. MPA-treated films show slower recombination rates with a narrower distribution compared to TA- and SA-treated films.

that the MPA-treated film showed a ~3 times longer carrier lifetime compared to the TA- and SA-treated samples. Using this general form of the PL intensity relaxation function to fit the PL decay, there are two advantages: (i) it is not necessary to choose an arbitrary number of exponential functions to describe the decay and (ii) the distribution of recombination rate constants (probability density function, H) can be obtained. It is clear that the perovskite film with the MPA treatment shows a slower recombination rate with a narrower distribution than those with the TA and SA treatments (Fig. 5b). This result suggests that perovskite films with a lower level of impurities at GBs have longer carrier lifetimes and slower intra-layer recombination rates with a narrower distribution.

Impedance spectroscopy (IS) measurements are performed on complete, planar PSCs with various post-annealing treatments to evaluate variations in V_{oc}, FF, PCE with the intra-layer and inter-layer carrier recombination. Measurements are performed under white LED illumination over a wide range of applied voltages and frequencies. Obtained IS spectra only contain two arcs and can be fitted using a simple equivalent electrical circuit (Fig. 6f).[56–59] Because the same structure and materials (*e.g.*, ETL and HTL) are used in the three different cases, observed differences can be attributed to the different quality of the perovskite films. From IS fittings, it is determined that the series resistance (R_s) is lower for the PSC with the MPA treatment compared to the TA or SA treatment (Fig. 6a), which facilitates charge transfer and leads to higher solar cell efficiency. The resistance extracted from the high frequency arc is assigned to the selective contact (R_{sc}), *i.e.* the contact between the ETL and perovskite, perovskite and the HTL, or the ETL and HTL. R_{sc} is higher for the PSC with MPA treatment compared to TA or SA

Table 1 Photovoltaic parameters of perovskite solar cells receiving TA, SA and MPA treatments respectively

	V_{oc} (V)	J_{sc} (mA cm^{-2})	FF (%)	PCE (%)
TA[a]	1.00 ± 0.02 (1.00)	19.6 ± 0.4 (19.5)	53.5 ± 2.9 (58.5)	10.5 ± 0.4 (11.4)
SA[a]	1.01 ± 0.01 (1.00)	19.6 ± 0.4 (19.6)	62.8 ± 3.0 (68.0)	12.5 ± 0.5 (13.3)
MPA[a]	1.05 ± 0.01 (1.04)	19.7 ± 0.3 (19.7)	72.6 ± 1.3 (75.2)	15.0 ± 0.2 (15.4)
TA[b]	1.05 ± 0.02 (1.09)	20.8 ± 0.8 (21.5)	73.8 ± 3.0 (78.7)	16.1 ± 0.7 (17.4)
MPA[b]	1.08 ± 0.02 (1.11)	20.8 ± 0.5 (21.6)	78.5 ± 1.7 (77.0)	17.7 ± 0.4 (18.4)

[a] Planar device. [b] Meso-structured device, () champion cell.

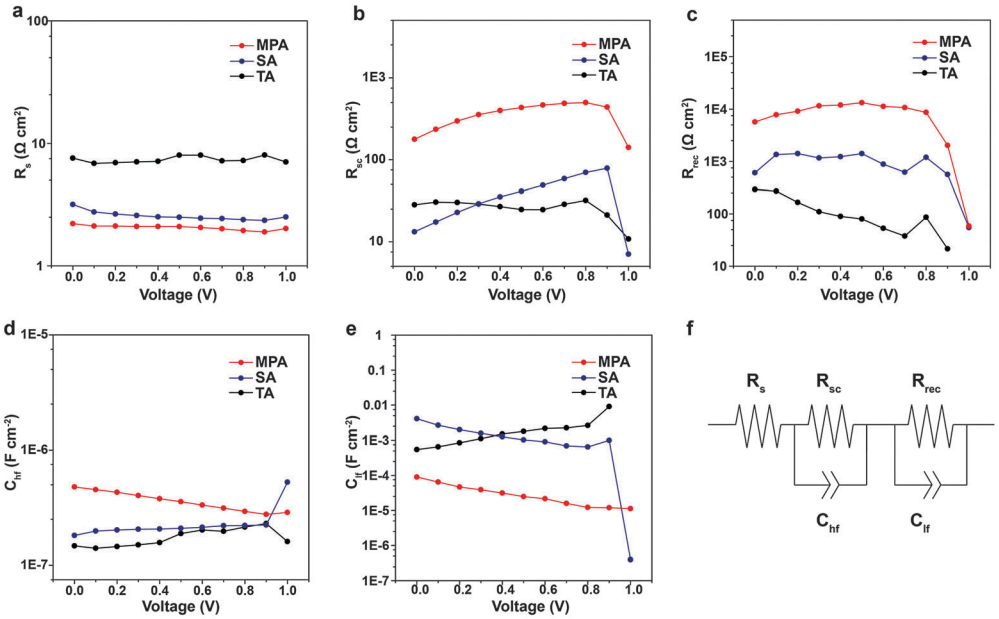

Fig. 6 Impedance spectroscopy of perovskite solar cells with various post-annealing treatments: (a) series resistance, (b) selective contact resistance, (c) recombination resistance, (d) high-frequency capacitance, (e) low-frequency capacitance and (f) equivalent circuit. MPA-treated perovskite solar cells show slower intra-layer and inter-layer recombination than TA- and SA-treated PSCs.

treatment (Fig. 6b). The higher R_{sc} is likely because the MPA treatment fuses the perovskite film, eliminating any possibility of direct contact between the ETL and the HTL. Hence the photo-generated carriers need to pass through a certain thickness of the perovskite film to achieve inter-layer carrier recombination, leading to an increase in R_{sc}. Another specific feature of the IS spectrum is the recombination resistance (R_{rec}), which is derived from the low frequency arc. MPA-treated PSCs exhibit more than 10 times higher resistance than TA- or SA-treated PSCs over nearly the entire range of studied voltage bias, indicating that the carrier recombination rate is significantly reduced (Fig. 6c). The capacitances from high frequency (C_{hf}) are similar for various post-annealing treatments (Fig. 6d). The C_{lf} associated in parallel with the R_{rec} shows an almost constant variation and lower profile in varying voltage for the MPA-treated samples compared with those treated with TA and SA suggesting that the MPA-treated samples contain a lower density of trap states, which leads to a lower charge recombination (Fig. 6e). The higher R_{rec} for the MPA-treated samples is in good agreement with their longer carrier lifetime (TRPL results). Therefore, R_{rec} is associated with intra-layer carrier recombination due to impurities at GBs, which explains why the MPA-treated perovskites achieve higher V_{oc} and FF.

The long-term stability of PSCs is of great importance, and it is highly related to the quality of the perovskite film.[60] Here, stability measurements are performed for planar PSCs with various post-annealing treatments. PSCs without encapsulation are kept in a dry cabinet (relative humidity ~15%) and measured in an ambient environment (relative humidity ~50%). After ten days, 93.1% of the initial device efficiency is obtained for the MPA-treated PSC while only 83.9% and 69.4% of the initial device efficiency is retained for the TA- and SA-treated PSCs, suggesting that the device stability is improved by the MPA treatment (Fig. 7a). Furthermore, steady state measurements are performed on both planar and meso-structured PSCs with TA and MPA treatments in an ambient environment. Note that the SA-treated sample was not included here because of its poor stability in an ambient environment. Measurements are also performed in an ambient environment on non-encapsulated devices and the applied voltage is actively adjusted to ensure that the devices are at the maximum power point. Both planar PSCs with TA and MPA treatments share double exponential efficiency decays, which agrees with a previous report (Fig. 7b).[61] The device treated with MPA shows a ~3 times slower degradation rate during the first rapid decay period compared with the TA-treated device, suggesting better stability. We believe that this observation is a result of higher quality of the perovskite film with better connected grains and fewer surface impurities at GBs, which leads to more tolerance to the local chemical environment. Similar decay kinetics appears at the second slow decay period, which is associated with the degradation of the perovskite or HTL under high humidity or because of TiO_2 related photo-induced degradation, since UV light is not filtered in this case. The device of thermally annealed, meso-structured PSCs shows a slightly slower degradation rate than that of thermally-annealed, planer PSCs. More interestingly, the meso-structured device with MPA treatment is substantially stable even in an ambient environment, with only 13.3% performance decay in 8000 s. This means that the MPA treatment can substantially improve the device stability independent of the device architecture. To further prove the concept, additional steady state measurements on TA- and MPA-treated PSCs are carried out in a N_2 filled glove box (relative humidity ~5%). Significantly improved device stabilities are achieved for both devices (Fig. 7c). PSC with TA treatment gives only 6.3% PCE decay in 8000 s, while MPA

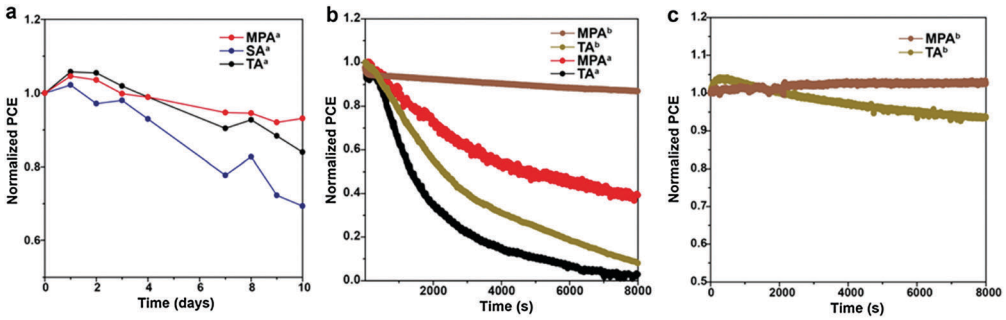

Fig. 7 Stability of perovskite solar cells with various post-annealing treatments. (a) Cells were kept in a dry cabinet in the dark and measured in ambient air. Cells were continuously measured at the maximum power point (b) in ambient air or (c) in a N_2 filled glove box of ~5% relative humidity. [a] For planar and [b] for meso-structured PSCs. MPA-treated PSCs show substantially slower degradation rates than TA- and SA-treated PSCs, independent of the device architectures.

treatment shows even a 2.7% PCE improvement. This PCE increase may relate to the light soaking effect.[62] This result suggests that the MPA treatment is even more promising if PSCs can be properly encapsulated.

Conclusions

In summary, the methylamine post-annealing treatment for $MAPbI_3$ perovskite is shown to reduce surface impurities at GBs and fuse disconnected grains. Both intra-layer recombination and inter-layer recombination are greatly suppressed, resulting not only in significant improvement of the performance of photovoltaic devices but also high reproducibility. This method works well for both planar and meso-structured perovskite solar cells and shows substantially improved device stability compared with other post-annealing treatments by improving the perovskite tolerance to the local chemical environment. It is anticipated that our method can be employed to enhance the perovskite film quality independent of the fabrication method employed for the initial film formation.

Acknowledgements

This work was supported by funding from the Energy Materials and Surface Sciences Unit of the Okinawa Institute of Science and Technology Graduate University and JSPS KAKENHI Grant Number 15K17925. We sincerely thank Prof. Nam-Gyu Park and Dae-Yong Son from Sungkyunkwan University for supplying the TiO_2 paste and giving helpful advice for making meso-structured perovskite solar cells. We thank Steven D. Aird, the Technical Editor, at Okinawa Institute of Science and Technology Graduate University (OIST) for valuable suggestions in revising the manuscript.

References

1 H. S. Kim, C. R. Lee, J. H. Im, K. B. Lee, T. Moehl, A. Marchioro, S. J. Moon, R. Humphry-Baker, J. H. Yum, J. E. Moser, M. Grätzel and N. G. Park, *Sci. Rep.*, 2012, **2**, 591.
2 J. Burschka, N. Pellet, S. J. Moon, R. Humphry-Baker, P. Gao, M. K. Nazeeruddin and M. Grätzel, *Nature*, 2013, **499**, 316–320.
3 M. Liu, M. B. Johnston and H. J. Snaith, *Nature*, 2013, **501**, 395–398.
4 H. Zhou, Q. Chen, G. Li, S. Luo, T. B. Song, H. S. Duan, Z. Hong, J. You, Y. Liu and Y. Yang, *Science*, 2014, **345**, 542–546.
5 W. Chen, Y. Wu, Y. Yue, J. Liu, W. Zhang, X. Yang, H. Chen, E. Bi, I. Ashraful, M. Grätzel and L. Han, *Science*, 2015, **350**, 944–948.
6 N. J. Jeon, J. H. Noh, W. S. Yang, Y. C. Kim, S. Ryu, J. Seo and S. I. Seok, *Nature*, 2015, **517**, 476–480.
7 W. Nie, H. Tsai, R. Asadpour, J. C. Blancon, A. J. Neukirch, G. Gupta, J. J. Crochet, M. Chhowalla, S. Tretiak, M. A. Alam, H. L. Wang and A. D. Mohite, *Science*, 2015, **347**, 522–525.
8 C. Yi, J. Luo, S. Meloni, A. Boziki, N. Ashari-Astani, C. Grätzel, S. M. Zakeeruddin, U. Röthlisberger and M. Grätzel, *Energy Environ. Sci.*, 2016, **9**, 656–662.
9 S. Wang, L. K. Ono, M. R. Leyden, Y. Kato, S. R. Raga, M. V. Lee and Y. B. Qi, *J. Mater. Chem. A*, 2015, **3**, 14631–14641.
10 National Renewable Energy Laboratory (NREL). http://www.nrel.gov/ncpv/images/efficiency_chart.jpg, accessed April, 2016.
11 Y. Zhao and K. Zhu, *J. Phys. Chem. Lett.*, 2014, **5**, 4175–4186.
12 T. Zhang, M. Yang, Y. Zhao and K. Zhu, *Nano Lett.*, 2015, **15**, 3959–3963.
13 L. K. Ono, S. Wang, Y. Kato, S. R. Raga and Y. B. Qi, *Energy Environ. Sci.*, 2014, **7**, 3989–3993.
14 H. S. Kim, S. H. Im and N. G. Park, *J. Phys. Chem. C*, 2014, **118**, 5615–5625.
15 B. Conings, L. Baeten, C. De Dobbelaere, J. D'Haen, J. Manca and H. G. Boyen, *Adv. Mater.*, 2014, **26**, 2041–2046.
16 J. Seo, S. Park, Y. Chan Kim, N. J. Jeon, J. H. Noh, S. C. Yoon and S. I. Seok, *Energy Environ. Sci.*, 2014, **7**, 2642–2646.
17 Y. Wu, A. Islam, X. Yang, C. Qin, J. Liu, K. Zhang, W. Peng and L. Han, *Energy Environ. Sci.*, 2014, **7**, 2934–2938.
18 C. Roldán-Carmona, P. Gratia, I. Zimmermann, G. Grancini, P. Gao, M. Grätzel and M. K. Nazeeruddin, *Energy Environ. Sci.*, 2015, **8**, 3550–3556.
19 G. E. Eperon, S. D. Stranks, C. Menelaou, M. B. Johnston, L. M. Herz and H. J. Snaith, *Energy Environ. Sci.*, 2014, **7**, 982–988.
20 P. W. Liang, C. Y. Liao, C. C. Chueh, F. Zuo, S. T. Williams, X. K. Xin, J. Lin and A. K. Jen, *Adv. Mater.*, 2014, **26**, 3748–3754.

21 Y. Zhao and K. Zhu, *J. Phys. Chem. C*, 2014, **118**, 9412–9418.
22 A. Mei, X. Li, L. Liu, Z. Ku, T. Liu, Y. Rong, M. Xu, M. Hu, J. Chen, Y. Yang, M. Grätzel and H. Han, *Science*, 2014, **345**, 295–298.
23 M. Xiao, F. Huang, W. Huang, Y. Dkhissi, Y. Zhu, J. Etheridge, A. Gray-Weale, U. Bach, Y. Cheng and L. Spiccia, *Angew. Chem., Int. Ed.*, 2014, **53**, 9898–9903.
24 N. J. Jeon, J. H. Noh, Y. C. Kim, W. S. Yang, S. Ryu and S. I. Seok, *Nat. Mater.*, 2014, **13**, 897–903.
25 Z. Xiao, Q. Dong, C. Bi, Y. Shao, Y. Yuan and J. Huang, *Adv. Mater.*, 2014, **26**, 6503–6509.
26 J. Liu, C. Gao, X. He, Q. Ye, L. Ouyang, D. Zhuang, C. Liao, J. Mei and W. Lau, *ACS Appl. Mater. Interfaces*, 2015, **7**, 24008–24015.
27 C. Liu, K. Wang, C. Yi, X. Shi, A. W. Smith, X. Gong and A. J. Heeger, *Adv. Funct. Mater.*, 2016, **26**, 101–110.
28 J. Li, J. Ma, Q. Ge, J. Hu, D. Wang and L. Wan, *ACS Appl. Mater. Interfaces*, 2015, **7**, 28518–28523.
29 J. S. Yun, A. Ho-Baillie, S. Huang, S. H. Woo, Y. Heo, J. Seidel, F. Huang, Y. Cheng and M. A. Green, *J. Phys. Chem. Lett.*, 2015, **6**, 875–880.
30 Y. Shao, Y. Fang, T. Li, Q. Wang, Q. Dong, Y. Deng, Y. Yuan, H. Wei, M. Wang, A. Gruverman, J. E. Shield and J. Huang, *Energy Environ. Sci.*, 2016, **9**, 1752–1759.
31 Q. Dong, Y. Fang, Y. Shao, P. Mulligan, J. Qiu, L. Cao and J. Huang, *Science*, 2015, **347**, 967–970.
32 B. Yang, O. Dyck, J. Poplawsky, J. Keum, A. Puretzky, S. Das, I. Ivanov, C. Rouleau, G. Duscher, D. Geohegan and K. Xiao, *J. Am. Chem. Soc.*, 2015, **137**, 9210–9213.
33 Y. Kato, L. K. Ono, M. V. Lee, S. Wang, S. R. Raga and Y. B. Qi, *Adv. Mater. Interfaces*, 2015, **2**, 26176.
34 W. Li, W. Zhang, S. Van Reenen, R. J. Sutton, J. Fan, A. A. Haghighirad, M. B. Johnston, L. Wang and H. J. Snaith, *Energy Environ. Sci.*, 2016, **9**, 490–498.
35 Y. Shao, Z. Xiao, C. Bi, Y. Yuan and J. Huang, *Nat. Commun.*, 2014, **5**, 5784.
36 Z. Zhou, Z. Wang, Y. Zhou, S. Pang, D. Wang, H. Xu, Z. Liu, N. P. Padture and G. Cui, *Angew. Chem., Int. Ed.*, 2015, **54**, 9705–9709.
37 S. Pang, Y. Zhou, Z. Wang, M. Yang, A. R. Krause, Z. Zhou, K. Zhu, N. P. Padture and G. Cui, *J. Am. Chem. Soc.*, 2016, **138**, 750–753.
38 T. Zhang, N. Guo, G. Li, X. Qian and Y. Zhao, *Nano Energy*, 2016, **26**, 50–56.
39 T. Zhang, N. Guo, G. Li, X. Qian, L. Li and Y. Zhao, *J. Mater. Chem. A*, 2016, **4**, 3245–3248.
40 S. R. Raga, M.-C. Jung, M. V. Lee, M. R. Leyden, Y. Kato and Y. B. Qi, *Chem. Mater.*, 2015, **27**, 1597–1603.
41 S. R. Raga, L. K. Ono and Y. B. Qi, *J. Mater. Chem. A*, 2016, **4**, 2494–2500.
42 Q. Chen, H. Zhou, Z. Hong, S. Luo, H.-S. Duan, H.-H. Wang, Y. Liu, G. Li and Y. Yang, *J. Am. Chem. Soc.*, 2014, **136**, 622–625.
43 A. Listorti, E. J. Juarez-Perez, C. Frontera, V. Roiati, L. Garcia-Andrade, S. Colella, A. Rizzo, P. Ortiz and I. Mora-Sero, *J. Phys. Chem. Lett.*, 2015, **6**, 1628–1637.
44 T.-W. Ng, C.-Y. Chan, M.-F. Lo, Z. Q. Guan and C.-S. Lee, *J. Mater. Chem. A*, 2015, **3**, 9081–9085.
45 W. Zhang, S. Pathak, N. Sakai, T. Stergiopoulos, P. K. Nayak, N. K. Noel, A. A. Haghighirad, V. M. Burlakov, D. W. deQuilettes, A. Sadhanala, W. Li, L. Wang, D. S. Ginger, R. H. Friend and H. J. Snaith, *Nat. Commun.*, 2015, **6**, 10030.
46 M.-C. Jung, Y. M. Lee, H.-K. Lee, J. Park, S. R. Raga, L. K. Ono, S. Wang, M. R. Leyden, B. D. Yu, S. Hong and Y. B. Qi, *Appl. Phys. Lett.*, 2016, **108**, 073901.
47 L. Liu, J. A. McLeod, R. Wang, P. Shen and S. Duhm, *Appl. Phys. Lett.*, 2015, **107**, 061904.
48 N. Aristidou, I. Sanchez-Molina, T. Chotchuangchutchaval, M. Brown, L. Martinez, T. Rath and S. A. Haque, *Angew. Chem., Int. Ed.*, 2015, **54**, 8208–8212.
49 P. Schulz, E. Edri, S. Kirmayer, G. Hodes, D. Cahen and A. Kahn, *Energy Environ. Sci.*, 2014, **7**, 1377–1381.
50 J. H. Heo, H. J. Han, D. Kim, T. K. Ahn and S. H. Im, *Energy Environ. Sci.*, 2015, **8**, 1602–1608.
51 H. Yoon, S. M. Kang, J. Lee and M. Choi, *Energy Environ. Sci.*, 2016, **9**, 2262–2266.
52 J. H. Heo, M. S. You, M. H. Chang, W. Yin, T. K. Ahn, S. Lee, S. Sung, D. H. Kim and S. H. Im, *Nano Energy*, 2015, **15**, 530–539.
53 Y. Jiang, B. B. Yu, J. Liu, Z. H. Li, J. K. Sun, X. H. Zhong, J. S. Hu, W. G. Song and L. J. Wan, *Nano Lett.*, 2015, **15**, 3088–3095.
54 Y. Jiang, X. Zhang, Q. Q. Ge, B. B. Yu, Y. G. Zou, W. J. Jiang, W. G. Song, L. J. Wan and J. S. Hu, *Nano Lett.*, 2014, **14**, 365–372.
55 M. N. Berberan-Santos, *Chem. Phys. Lett.*, 2008, **460**, 146–150.
56 E. J. Juarez-Perez, M. Wußler, F. Fabregat-Santiago, K. Lakus-Wollny, E. Mankel, T. Mayer, W. Jaegermann and I. Mora-Sero, *J. Phys. Chem. Lett.*, 2014, **5**, 680–685.
57 J. Zhang, E. J. Juárez-Pérez, I. Mora-Seró, B. Viana and T. Pauporté, *J. Mater. Chem. A*, 2015, **3**, 4909–4915.
58 V. Gonzalez-Pedro, E. J. Juarez-Perez, W. S. Arsyad, E. M. Barea, F. Fabregat-Santiago, I. Mora-Sero and J. Bisquert, *Nano Lett.*, 2014, **14**, 888–893.
59 O. A. Jaramillo-Quintero, M. Solis de la Fuente, R. S. Sanchez, I. B. Recalde, E. J. Juarez-Perez, M. E. Rincon and I. Mora-Sero, *Nanoscale*, 2016, **8**, 6271–6277.
60 N. Ahn, D. Y. Son, I. H. Jang, S. M. Kang, M. Choi and N. G. Park, *J. Am. Chem. Soc.*, 2015, **137**, 8696–8699.
61 A. Abate, S. Paek, F. Giordano, J.-P. Correa-Baena, M. Saliba, P. Gao, T. Matsui, J. Ko, S. M. Zakeeruddin, K. H. Dahmen, A. Hagfeldt, M. Grätzel and M. K. Nazeeruddin, *Energy Environ. Sci.*, 2015, **8**, 2946–2953.
62 C. Zhao, B. Chen, X. Qiao, L. Luan, K. Lu and B. Hu, *Adv. Energy Mater.*, 2015, **5**, 1500279.